Soft Matter

Patterning non-equilibrium morphologies in stimuli-responsive gels through topographical confinement

Journal:	*Soft Matter*
Manuscript ID	SM-ART-11-2019-002221.R1
Article Type:	Paper
Date Submitted by the Author:	04-Dec-2019
Complete List of Authors:	Zhang, Cathy; Harvard University, Liu, Ya; University of Pittsburgh Wang, Xinran ; University of Waterloo Wang, Xiaoguang; Ohio State University Kolle, Stefan; Harvard University Balazs, Anna; University of Pittsburgh, Chemical Engineering Aizenberg, Joanna; Harvard,

SCHOLARONE™
Manuscripts

Soft Matter

Patterning non-equilibrium morphologies in stimuli-responsive gels through topographical confinement†

Cathy T. Zhang[*a], Ya Liu[b], Xinran Wang[c], Xiaoguang Wang[d], Stefan Kolle[a], Anna Balazs[b], Joanna Aizenberg[a]

Stimuli-responsive "smart" polymers have generated significant interest for introducing dynamic control into the properties of antifouling coatings, smart membranes, switchable adhesives and cell manipulation substrates. Switchable surface morphologies formed by confining stimuli-responsive gels to topographically structured substrates have shown potential for a variety of interfacial applications. Beyond patterning the equilibrium swelling behavior of gels, subjecting stimuli-responsive gels to topographical confinement could also introduce spatial gradients in the various timescales associated with gel deformation, giving rise to novel non-equilibrium morphologies. Here we show how by curing poly(N-isopropylacrylamide) (pNIPAAm)-based gel under confinement to a rigid, bumpy substrate, we can not only induce the surface curvature to invert with temperature, but also program the transient, non-equilibrium morphologies that emerge during the inversion process through changing the heating path. Finite element simulations show that the emergence of these transient morphologies is correlated with confinement-induced gradients in polymer concentration and position-dependent hydrostatic pressure within the gel. To illustrate the relevance of such morphologies in interfacial applications, we show how they enable us to control the gravity-induced assembly of colloidal particles and microalgae. Finally, we show how more complex arrangements in particle assembly can be created through controlling the thickness of the temperature-responsive gel over the bumps. Patterning stimuli-responsive gels on topographically-structured surfaces not only enables switching between two invertible topographies, but could also create opportunities for stimuli ramp-dependent control over the local curvature of the surface and emergence of unique transient morphologies. Harnessing these features could have potential in the design of multifunctional, actuatable materials for switchable adhesion, antifouling, cell manipulation, and liquid and particle transport surfaces.

1 Introduction

Stimuli-responsive materials[1–3] have found applications in fields as diverse as drug delivery[4], actuators[5], smart membranes[6], switchable adhesives[7], antibacterial surfaces[8] and cell manipulation substrates[9–11]. Hybrid or composite surfaces, in which soft and responsive materials are covalently bonded with static components that prescribe how soft materials mold, conform, and deform, often provide emergent functionality that cannot

be achieved with either component alone[12–16]. For example, stimuli-responsive hydrogels are an interesting class of responsive materials[17] that change their volume with stimuli such as temperature, electric field, light, or pH, resulting in changes in surface porosity, adhesiveness, mechanical properties, charge, and wettability. Curing such gels to rigid topographical features, such as vertically aligned carbon nanotubes[18], prestructured surfaces[19,20], or a layer of colloidal silica[14] alters the mechanical boundary conditions, introducing anisotropy into the deformation process and creating new surface functionality (e.g. switchable self-cleaning properties[18], dynamic display of biomolecular patterns[19], and particle manipulation and transport[14,19]). While it has experimentally been observed that gel shrinking can lead to non-equilibrium pattern formation[21] on the surfaces of bulk cylindrical gels[22–25], microgels[26,27], flat surfaces[28] and tori-shaped gels[29], these phenomena remain unexplored in hybrid

[a] Harvard University School of Engineering and Applied Sciences, Cambridge, MA, USA.
Tel: (617) 496-8381; E-mail: cathyzhang@g.harvard.edu
[b] University of Pittsburg, Pittsburg, PA, USA.
[c] Unversity of Waterloo, Waterloo, Ontario, Canada.
[d] Ohio State University, Cleveland, Ohio, USA.

surfaces consisting of responsive gels cured to prestructured topographical features. Programming non-equilibrium behavior in hybrid surfaces could introduce more flexible control over the patterning and manipulation of colloidal particles[30–32], microorganisms[33,34], and mammalian cells[8,11], all of which are highly sensitive to local changes in the mechanical, topographical, and chemical properties of surfaces.

Subjecting stimuli-responsive gels to topographical confinement has the potential to introduce spatial gradients in the various timescales associated with gel deformation, which could introduce new transient mechanical constraints and the formation of surface instabilities. In order to study these effects, we investigated transient surface morphologies in a hybrid surface consisting of a temperature-responsive hydrogel based on poly(N-isopropylacrylamide) (pNIPAAm, lower critical solution temperature 32 °C) that is covalently cured to a rigid surface patterned with bumps and crevices (see schematic at top of Fig 1). To accentuate the effect of spatial gradients in gel response timescales, the gel is UV-polymerized onto a topographically patterned surface with large, periodically spaced bumps (150 μm in height and 500 μm in width) under a flat confining surface that causes the post-fabrication gel height at each point to be inversely correlated with the height of the underlying bumps. Upon immersing in water and releasing the confining upper surface, the gel swells to exhibit large gradients in height as it shrinks and swells with temperature.

Here we show how by topographically confining the gel in this manner, we can not only induce the surface curvature to invert with temperature, but also program the transient, non-equilibrium morphologies that emerge during the inversion process through changing the heating path. We use a combination of timelapse fluorescence confocal microscopy and finite element simulations to visualize and compare the surface morphology during heating between three different setpoint temperatures under two different kinetic regimes (details provided in Fig 1). To illustrate the potential utility of transient morphologies in interfacial applications, we deposit colloidal particles and *C.reinhardtii* microalgae onto the surface in order to show how a combination of surface inversion and non-equilibrium morphology transformations enables us to reconfigure the gravity-induced assembly of particles and microalgae in a heating-path dependent manner. Finally, we harness insights gained from experiments and finite element simulations to design more complex trajectories in the assembly of sedimenting colloidal particles and elicit non-trivial colloidal patterning.

2 Materials and Methods

2.1 Materials

Lenticulated plastic sheets (50 lines per inch, with bump-to-bump pitch ≈500 μm) were purchased from Pacur and Lenstar. Sylgard 184 polydimethylsiloxane base and curing agent were purchased from Sylgard. Epoxy OG178 was purchased from Epotek. Trichloro(1H,1H,2H,2H-perfluorooctyl)silane (13F-silane), glycidyl methacrylate (GMA), polyethylene glycol diacrylate (PEGDA, Mn700), Darocur 1173, ethylene glycol and
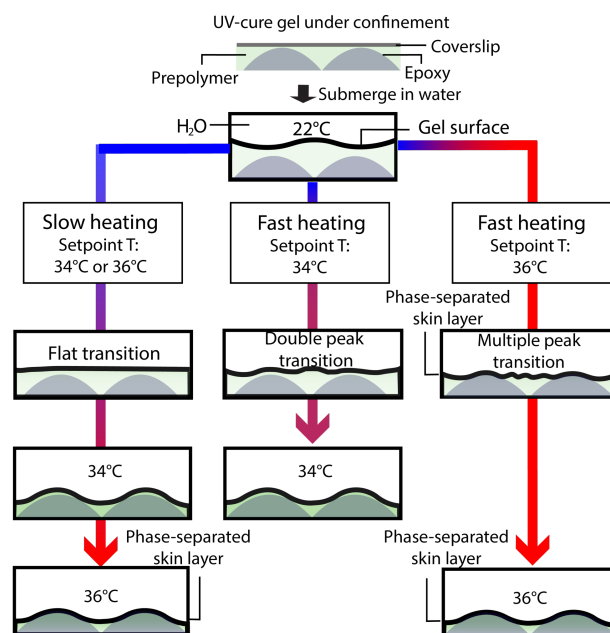
Fig. 1 Overview of experimental system consisting of temperature-responsive gel prepolymer UV-cured under confinement between a flat surface and a topographically patterned epoxy surface, as viewed from the side. Comparison between morphologies obtained in the slow heating regime (heating rate R=0.2 °C/min) to setpoint temperatures of either T_{sp}=34 °C or 36 °C (left) and morphologies obtained through the fast heating regime (R=5 °C/min) and subsequent relaxation at T_{sp}=34 °C (center) and 36 °C (right). The surface morphology at each stage has been emphasized in black.

1-butanol were used directly as received from Sigma Aldrich. Pyrromethene dye 546 was obtained from Exciton. *N*-isopropylacrylamide (NIPAAm) monomer was purchased from Sigma Aldrich and recrystallized in 1:1 hexane/toluene mixture overnight at 4 °C to remove impurities. Alkyne-functionalized BODIPY-R6G fluorescent dye was purchased from Lumiprobe. Silicone spacers were obtained from Grace Biolabs. 10 μm diameter FITC-labeled carboxylated melamine particles were purchased from Fluka. UTEX90 algae and Bristol media and soil extract were obtained from UTEX Culture Collection of Algae. Propidium iodide and Syto 9 were obtained from Invitrogen.

2.2 Molding rigid epoxy bumps from lenticulated plastic sheets

Rigid bumps were created through curing glycidyl methacrylate-embedded OG178 epoxy (10 w/v % GMA in OG178 epoxy) under an inverse mold of the lenticulated plastic bumps. For fluorescently labeled samples used for imaging, 5 vol% of the epoxy component was replaced with OG178 saturated with pyrromethene dye. Lenticular lens plastic sheets (50LPI) were plasma cleaned, vapor silanized with 13F silane under desiccated vacuum conditions and used as masters for molding. PDMS (Sylgard, base:curing 10:1) was poured onto the masters, cured for 2 h at 70 °C and peeled off the plastic bumps to reveal PDMS inverse

replicas of the bumps. A 50 μm base layer of epoxy mixture was UV-cured (Dymax Model 2000 Flood UV Curing System, light intensity of $\approx$18 mW/cm^2 for 5 min) under the confinement of a PDMS slab onto 22 mm plasma-treated square glass coverslips. After peeling the PDMS slab off the surface, epoxy bumps were fabricated on the epoxy base by pressing 1cm square PDMS inverse replicas of lenticulated bump stuctures to the surface and infiltrating with epoxy-GMA mixture through capillary filling. The ensemble was UV-cured for 5 min and the PDMS molds were subsequently peeled off.

2.3 Fabrication of fluorescently labeled pNIPAAm gel on epoxy bumps

NIPAAm monomer was UV-polymerized with crosslinker PEGDA, Darocur 1173 and covalently labeled with BODIPY-R6G dye in the channels formed by sandwiching the rigid epoxy bumps under a glass coverslip. NIPAAm and PEG-based crosslinker were chosen because surfaces containing these two components have been widely explored for interfacial applications[30,35,36]. Moreover, the GMA embedded within the epoxy bumps enables it to be covalently grafted with the gel, while a small portion of the alkyne-functionalized fluorescent dye is expected to be conjugated directly into the gel network via free radical addition[37]. Here we use the acronym NIPAAm to denote the monomer, while pNIPAAm is used to denote the polymerized form, i.e. poly(*N*-isopropylacrylamide).

Prepolymer solutions were made in a solvent mixture of 1:1 mixture of 1-butanol and ethylene glycol by volume to facilitate complete wetting of the hydrophobic epoxy microstructures. For all solutions, the molar ratio of NIPAAm to crosslinker PEGDA was fixed at $\phi_{crosslinking} = \frac{C_{PEGDA}}{C_{NIPAAm}} = 1.6\%$. First, concentrated stock solution containing C_{NIPAAm}=6.7 M and $\phi_{crosslinking} = \frac{C_{PEGDA}}{C_{NIPAAm}} = 1.6\%$ was prepared by dissolving 367 mg recrystallized NIPAAm powder and 33 μl of PEGDA in 484 μl of solvent. Dye stock solutions were prepared by saturating the solvent with dye at 22 °C. All stock solutions were stored at 4 °C until use. Just prior to sample fabrication, prepolymer working solutions were created by mixing NIPAAm stock solutions with Darocur and solvent to nominal values: (1) NIPAAm molar concentration C_{NIPAAm}=1.98 M, 3.3 M or 5.94 M, (2) 2 mol % Darocur, and (3) 10 vol% dye stock. For example, to create 200 μl working solution with C_{NIPAAm}=3.3 M: 100 μl NIPAAm stock was diluted with 80 μl solvent, 20 μl dye stock and 4 μl Darocur. For non-fluorescently labeled samples used in particle assembly experiments, dye stock solution was replaced with solvent. To fabricate the hybrid surface, prepolymer working solution was infiltrated into the channels formed by sandwiching the epoxy bumps with a precut 9mm square glass coverslip, then UV-cured through the coverslip for 5 min. Samples were then fully submerged in Millipore DI water for at least 30 min, and the coverslip was gently released manually to allow overnight hydrogel swelling and solvent exchange. Samples were thoroughly rinsed with DI water immediately prior to experiments.

2.4 Confocal measurements of surface morphology

To visualize changes in surface morphology that occur as the temperature is changed, the sample was imaged in a thin flowcell with a glass window (channel height over the surface $h_{channel}$ $\approx$350 μm) placed on a feedback-controlled resistive heating stage controlled by a PID temperature controller (Instec STC200 precision temperature controller) and cooled by water pumped from an ice-water bath (T=0 °C). Prior to all experiments, the top of the stage was carefully calibrated with a digital thermometer (Omega HH1384) equipped with a K-type thermocouple to within $\pm$0.3 °C of the setpoint temperature indicated on the temperature controller. For each experiment, the heating stage was heated or cooled to predetermined temperature setpoints (e.g. T_{sp}=34 °C or 36 °C) at controlled heating rates (R=0.2 °C/min and 5 °C/min). Because the glass coverslip on which the hybrid surface is made is sufficiently thin, the entire flowcell equilibrates to the temperature of the heating stage within a few seconds. To obtain side view cross-section images, timelapse images of fluorescence confocal z-stack images were collected at specified time intervals (Zeiss upright LSM 510, 20x water objective, 0.5NA, λ_{ex}=488 nm, 1 Airy unit pinhole) with separate channels for reflected laser light ($\lambda \approx$488 nm), fluorescently labeled epoxy (pyrromethene 546), and hydrogel fluorescence (BODIPY-R6G). For image analysis, a custom script was written in FIJI and MATLAB for thresholding and extracting surface profiles. To obtain top-view images, samples were imaged under similar lighting settings with a wider pinhole in both fluorescence and reflection modes at 2 s intervals.

2.5 Finite element simulations

We implement our gel lattice spring model (gLSM), which is a finite element approach for solving the spatially discretized equations for the elastodynamics of the gel[38–40]. In the framework of gLSM, a 3D deformable gel is represented by a set of general linear hexahedral elements, and the structural evolution of the local volume fraction of polymer, ϕ, is governed by the continuity equation:

$$\frac{\partial \phi}{\partial t} = \nabla \cdot (\phi v^p), \qquad (1)$$

where v^p is the polymer velocity (details of gLSM in Supplementary Information). In the simulation, we set the units of length (i.e. edge of each grid cell) and time to correspond to $L_0 = 5\,\mu$m and $t = 1.25$ s, respectively in physical units, to ensure the diffusion coefficient 2×10^{-11} m^2/s[16,40]. Initially, the gel sample is undeformed and consists of $(L_x - 1) \times (L_y - 1) \times (L_z - 1)$ identical cubic elements, where $L_x = 101, L_y = 11$ and $L_z = 32$ is the number of nodes in the corresponding direction; the linear size of the elements in the undistorted state with $\phi_0 = 0.1286$ is set to $L_0 = 1$. The solid bump is modeled as frozen gel nodes by setting their velocities to zero and polymer volume fraction $\phi = 1$. Further details are provided in ESI†.

2.6 Gravity-induced particle assembly experiments

Fluorescent carboxylated melamine particles (diameter: 10 μm, negatively-charged, FITC-labeled) were centrifuged in 1.6 ml polypropylene Eppendorf tubes and diluted in DI water to

0.3 wt%. A fluid well was assembled by layering a precut acrylic adhesive-backed silicone gasket (Grace Biolabs) on top of a 1mm-thick glass slide. $100\,\mu l$ of particle solution was injected into the well and the as-prepared surfaces fabricated on 22mm square coverslips were layered upside down over the fluid well. Just prior to experiments, samples were flipped over and the particles were allowed to settle onto the gel surface (t$\sim$3 min for carboxylated melamine particles, density $\rho = 1.5\,\mathrm{g/ml}$). Once assembled, the channel height over the surface $h_{channel}$ was $\approx 350\,\mu m$. The surface was then heated to predetermined temperature setpoints $T_{sp}=33$, 34, or 36 °C at a controlled heating rate of R=5 °C/min, and particle trajectories were captured using a fluorescence microscope (Zeiss, 10X objective) for 10 min at 10 s intervals. For experiments with *C.reinhardtii* microalgae, *C.reinhardtii* UTEX90 cells obtained from University of Texas were used for the biological cell assembly experiments. Prior to experiments, cells were cultivated at room temperature (20 °C) under Sun Blaze T5HO fluorescent light fixtures equipped with Spectralux 6500 K T5 HO Lamps. Cell cultures were subjected to a 16h light/8h dark illumination cycle in 1000 ml autoclave-sterilized, aerated Erlenmeyer flasks containing 750-800 ml of Bristol media. Fresh media was supplied once every 7 days. Just prior to experiments, cells were washed *via* centrifugation at 3000 rpm for 5 minutes in 15 ml Falcon tubes and concentrated to a cell count of 25 million cells/ml in Bristol media. Algal suspension was injected into a channel that was assembled as described previously. After allowing algae to settle for 15 min, the sample was heated to $T_{sp}=35.5$ °C at a rate of R=2.5 °C/min and algae trajectories were captured using a fluorescence microscope (Zeiss) for 15 min at 10 s intervals. Here, the setpoint temperature and heating rate were reduced slightly to decrease the mortality rate of microalgae and degree of convective flow within the flowcell. Through dead staining of microalgae using Sytox Green, we observe that at a temperature of 35.5 °C, close to 100% of microalgae are alive (data not shown).

3   Results and Discussion

3.1   In the slow heating regime, the gel surface inverts by passing through a flat transition state.

We first explored the morphologies attainable through a fluorescently labeled, hybrid temperature-invertible surface in the slow-heating regime, where the morphology is expected to be close to thermodynamic equilibrium. These surfaces were fabricated by UV-initiated co-polymerization of *N*-isopropylacrylamide (NIPAAm), polyethylene glycol diacrylate (PEGDA), and BODIPY-R6G dye on a bumpy surface under the confinement of a glass coverslip (procedural details are included in Materials and Methods and ESI-1A). The bumps were 150μm in height, 500μm in width, replicated in epoxy and doped with glycidyl methacrylate (GMA) before curing to enable covalent attachment to the acrylate-based hydrogel and prevent delamination. In order to distinguish between the gel bound to different locations on the epoxy bump, gel bonded to the bump apex are hereto referred to as being at "bump sites" (with lateral coordinate x=0 μm), while gel bonded to the epoxy grooves are at "crevice sites"

(x=$\pm250\,\mu$m). Due to the temperature-sensitive transition of polymerized pNIPAAm at its lower critical solution temperature, at thermodynamic equilibrium, pNIPAAm-based gel films typically exhibit an equilibrium gel height h_{eq} that is proportional to its as-fabricated, preswollen gel height $h_{preswollen}$ and a swelling ratio ε that is dependent on temperature T:

$$h_{eq}(T) = h_{preswollen}\varepsilon(T) \qquad (2)$$

While this equation is only strictly valid in the case where the gradient of height in the gel film is small and lateral deformation of the gel surface is not significant, it suggests that the gel at the crevice sites will undergo more drastic temperature-dependent changes in height than that at the bump sites. As the exact form of $\varepsilon(T)$ is typically dependent on the gel composition (e.g. degree of ionization and polymer density), we tested three different NIPAAm concentrations $C_{NIPAAm}=1.98$ M, 3.3 M, and 5.94 M, while fixing $\phi_{crosslinking}$ at 1.6% because the surface and mechanical properties of gels with this crosslinking ratio are well-studied and relevant for interfacial applications such as antifouling[41,42]. Samples polymerized with these NIPAAm concentrations were mechanically robust during the fabrication process against tearing and deformation, and no delamination of the gel from the substrate was observed up to 60 °C.

For each gel composition, we visualized the temperature-dependent surface profile *via* confocal fluorescence microscopy by heating the surface at a slow rate of R=0.2 °C/min from 22 °C to 36 °C while taking a z-stack image every 5 min. Each stack consisted of 145 slices in z, 512 pixels in x, and y=65 pixels. Each stack took just under 30 sec to acquire. Typical temperature-dependent z-stack images and surface profiles obtained for samples containing $C_{NIPAAm}=3.3$ M at 22 °C, 31 °C, 34 °C, and 36 °C are shown in Fig 2A-B, while images for gels containing $C_{NIPAAm}=1.98$ M and 5.94 M are included in ESI†(Fig S1B).

For all gel compositions tested, order-of-magnitude differences in preswollen gel height at bump sites ($h_{preswollen}$(x=$\pm250\mu$m)$\approx$ 150μm) vs crevice sites ($h_{preswollen}$(x=0)$\approx$ 10μm) cause the gel surface to swell and contract to varying total heights $h_{eq}(T)$ upon cooling and heating, forming prominent ridges that gradually flatten and eventually invert with temperature to form crevices. At 22 °C, the height of the gel protrudes to $\approx 40\mu$m, $\approx 50\mu$m, and $\approx 60\mu$m above the epoxy bump for $C_{NIPAAm}=$ 1.98 M, $C_{NIPAAm}=$ 3.3 M and $C_{NIPAAm}=$ 5.94 M, respectively. Upon increasing the temperature to 36 °C, the gel collapses to 40μm, 30μm, and 20μm below the epoxy bump for $C_{NIPAAm}=$ 1.98 M, $C_{NIPAAm}=$ 3.3 M and $C_{NIPAAm}=$ 5.94 M, respectively. The temperature at which the upper surface undergoes a transition through a flat configuration increases slightly with C_{NIPAAm}, due to gel composition-dependent differences in the function $\varepsilon(T)$ mentioned above.

Confocal fluorescent images show that for samples with $C_{NIPAAm}=$ 3.3 M and 1.98 M (ESI†Fig S1B), the polymer density through the depth of the gel is approximately uniform until the gel reaches a critical temperature of $\approx$35 °C and $\approx$34 °C for $C_{NIPAAm}=3.3$ M and $C_{NIPAAm}=1.98$ M, respectively. At these critical temperatures, the homogeneous gel segregates into a skin

layer that is polymer-rich, as evidenced by the higher fluorescent intensity, and a bulk region underneath that is polymer-poor. This skin layer becomes particularly evident at 36 °C. The formation of a skin layer is more gradual and less clearly defined for gels containing $C_{NIPAAm} = 5.94M$ (ESI†, Fig S1C-E). This is consistent with previous reports indicating that thermoresponsive gels synthesized with higher C_{NIPAAm} exhibit a more continuous volume phase transition and either do not phase separate[43] or phase separate at higher temperatures than networks with lower C_{NIPAAm}[24]. Because phase separation is expected to be important for the formation of non-equilibrium patterns on collapsing gels[23,44,45], we focused on the gel containing C_{NIPAAm}=3.3 M for the rest of this study.
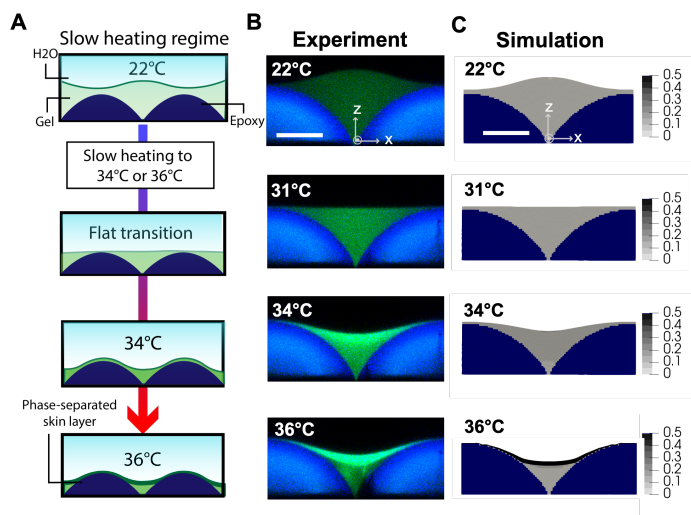
Fig. 2 Slow heating regime: Surface morphology and polymer density distribution in the gel when the surface is heated at heating rate R=0.2 °C/min to 34 °C or 36 °C. A. Schematic showing sequence of gel surface inversion and skin layer phase separation with increasing temperature. B. Confocal images (blue: rigid bumps, green: pNIPAAm gel) show inversion of surface curvature with temperature and formation of phase-separated skin layer at the surface at 36 °C. Experimental images have been convoluted with 1 pixel Gaussian blur to reduce noise. Scale: 125 μm. C. gLSM simulations show inversion of curvature with temperature between T=22 °C and 34 °C and the emergence of a distinct phase separated skin layer (polymer volume fraction ϕ=43%) between T=34 °C and 36 °C. Color bar represents polymer volume fraction. Scale: 125 μm.

To verify that the skin layer we observed in experiments for this gel composition was at thermodynamic equilibrium and gain further understanding into how topographical confinement influences the gel mechanics with temperature, we used gel lattice spring model (gLSM) finite element simulations to characterize the system. The surface profiles obtained from simulations at each temperature agree with the experimentally measured morphologies. As shown in Fig 2C, the surface profile of the swollen gel ($T = 22$ °C), flat transition ($T = 31$ °C), and collapsed gel ($T = 34$ °C and $T = 36$ °C) agree with experimental results shown in Fig 2B. The corresponding color bar represents the polymer volume fraction within the gel. Notably, the polymer volume fraction distribution is also consistent with experiments: at 34 °C, the highest polymer volume fraction ϕ appears

at the top surface of the gel (between 7 and 13%), with a slight increase in ϕ from the bump sites toward the crevice sites. At 36 °C, the gel is phase-separated into an upper skin-layer region of high polymer volume fraction ($\phi \approx 43\%$) and a lower region of low polymer volume fraction ($\phi < 10\%$). The stratification of the gel into two distinguishable phases can be attributed to the fact that the gel underneath the skin layer is under tension, which enables the thermodynamically stable coexistence of two separate phases[46,47]. Overall, the good agreement in both surface profile and polymer volume fraction distribution between simulation and experiment suggests that the main features of the hybrid surface are captured by the model described above.

3.2 In the fast heating regime, the surface inverts by passing through either a double-peak or multiple-peak transition state.

To investigate the fast-heating regime, we experimentally increased the rate at which the substrate was heated, and allowed the surface to relax at fixed setpoint temperatures T_{sp}. We compared two different cases: (1) under conditions where phase separation is minimal, i.e. when the gel relaxes at a temperature $T_{sp} \approx 34$ °C, and (2) under conditions where phase separation is expected to occur ($T_{sp} \approx 36$ °C).

When the gel is allowed to relax at a temperature below the phase separation temperature, the gel shrinkage is governed by the collective diffusion of polymer relative to the solvent, and thus the rate of gel contraction would scale roughly inversely proportionally to the dimension of the gel squared[27]. Assuming water flux occurs solely in the z direction through the surface of the gel, the characteristic time to reach equilibrium for each point in the gel could be approximated as $t_{eq} \approx \frac{h^2}{D_{coop}}$, where D_{coop} is on the order of $10^7 \, \text{cm}^2/\text{s}$[22]. Due to differences in equilibrium height (h_{eq}) of the gel between the crevice and bump sites at all temperatures, the ratio of equilibration times for the gel at each site on introducing a temperature impulse from T to T_{sp} should scale approximately as:

$$\frac{t_{eq,crevice}}{t_{eq,bump}} \approx \left(\frac{h_{eq,crevice}(T_{sp}) - h_{eq,crevice}(T)}{h_{eq,bump}(T_{sp}) - h_{eq,bump}(T)} \right)^2 \quad (3)$$

Thus, using the height changes observed in Fig 2B, we obtain an estimate of $\frac{t_{eq,crevice}}{t_{eq,bump}} \approx 64$; that is, in an idealized scenario, we would expect the gel at bump sites to reach equilibrium 64 times faster than gel at crevice sites. While confinement of the gel could drive water to move laterally within the gel in addition to perpendicularly out through the surface, this analysis suggests that at high heating rates, the deswelling rate of the pNIPAAm gel would also be dependent on the relative height of the gel, which could give rise to additional transient morphologies.

On the other hand, when the gel is allowed to relax at a temperature at or above the phase separation temperature (e.g. at 36 °C or 38 °C), a similar contraction process is expected to occur, but the timescale for the contraction of the gel bulk further competes with the formation of a skin layer. We expected that confinement of thermoresponsive gels onto a bumpy surface could introduce spatial gradients in shrinking rates while forc-
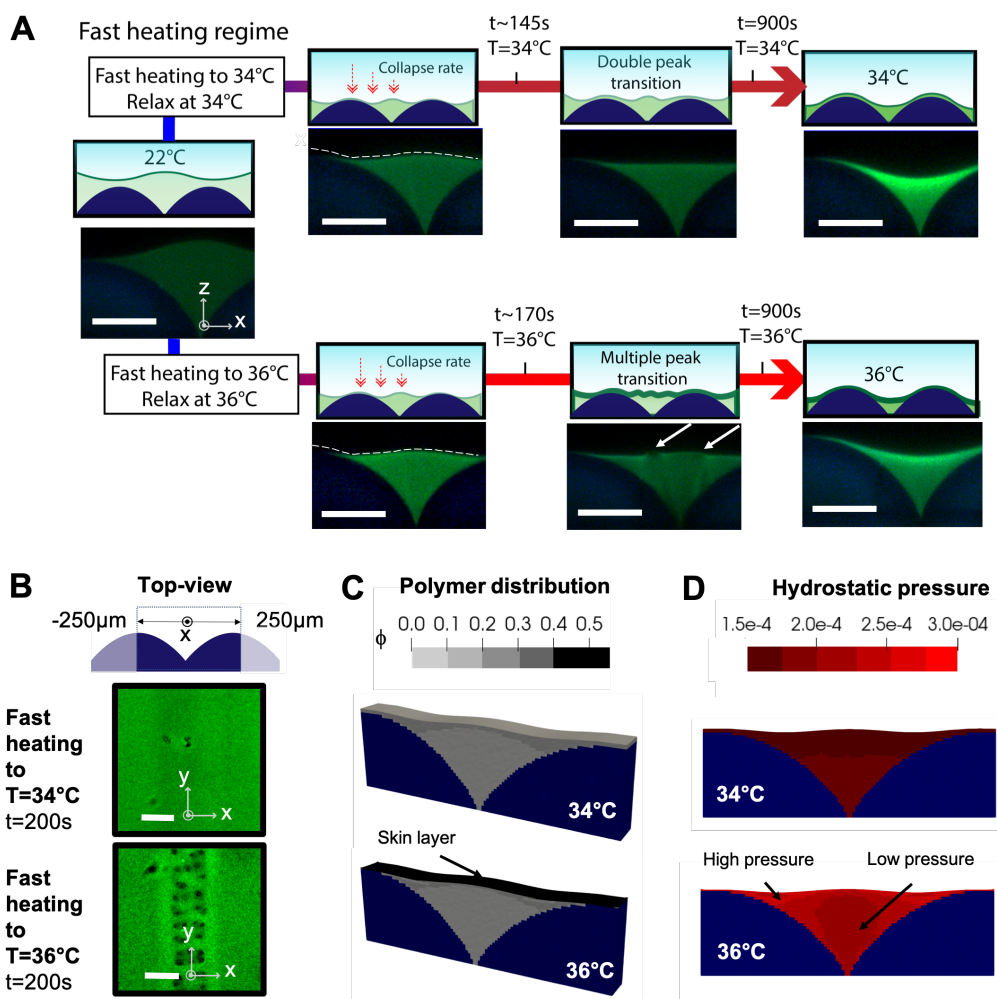
Fig. 3 Fast heating regime: Surface inversion during heating at a rate of R=5 °C/min and subsequent relaxation at T_{sp} =34 °C vs 36 °C. A. Schematic and representative z confocal stack images illustrating the difference between allowing the gel to relax after fast heating at R=5 °C/min to T_{sp}=34 °C vs T_{sp}=36 °C. The gel reaches the setpoint temperature within ≈145 s and ≈170 s for T_{sp} =34 °C and 36 °C, respectively. Moreover, the gel begins to contract from the bump sites in all cases and goes through a transition with two peaks. When T_{sp} = 36 °C, small bulges (or bubbles) appear in the surface, forming multiple peaks. On the other hand, when T_{sp} = 34 °C, the surface contracts smoothly to inversion. Confocal images have been convoluted with 1 pixel Gaussian blur to reduce noise. Scale: 125 μm. B. Representative topview confocal images comparing the process of surface inversion for T_{sp} =34 °C and 36 °C (t =200 s). Scale: 125 μm. C. Gel lattice spring model (gLSM) simulations for the surface inversion process in the fast heating regime to T_{sp}=34 °C and 36 °C. Note the formation of a very thin skin layer in the case when T_{sp}=36 °C and inhomogeneities in gel concentration underneath the skin layer. D. Hydrostatic pressure profile within the gel indicates the presence of a low pressure region in the bulk of the gel, suggesting that water is forced to migrate laterally in the x direction toward the crevice sites during gel collapse, eventually building up sufficient pressure to escape through the skin layer over the crevice sites. By contrast, for T_{sp}=34 °C, the hydrostatic pressure profile only exhibits gradients in the z direction.

ing a phase-separated skin layer to undergo a macroscopic switch from positive to negative curvature.

To explore these effects, we visualized and compared the transient morphologies of the gel surface during heating at a rate of R=5 °C/min from 22 °C to setpoint temperatures T_{sp} = 34 °C, 36 °C and 38 °C through confocal fluorescence z-stack imaging. Representative images obtained for T_{sp} = 34 °C and 36 °C are provided in Fig 3A, while the full dataset for all three conditions is presented in ESI†(Fig S2A). Under the heating conditions used in our study, the gel reaches the setpoint temperature within ≈145 s to 190 s and gels do not reach an inverted state within this timeframe.

In all cases, gels shrink most quickly at the bump sites from t=0, forming two crevices adjacent to the bump sites as shown in the Fig 3A. This is in contrast to the gel in the slow heating regime, which goes through a flat transition and thus a no-peak transition (as seen in Fig 2B). As shown in the top row of Fig 3A, R=5 °C/min and T_{sp} =34 °C, the gel reaches 34 °C within t≈145 s, then continues to contract smoothly to inversion. On the other hand, for T_{sp} =36 °C (shown in the bottom row of Fig 3A) or 38 °C (shown in SI), the gel reaches the setpoint temperature within t≈170 s or t≈190 s, respectively, after which a thin, polymer-rich skin layer begins to appear at the upper surface of the gel. Moreover, at t≈200 s, noticeable inhomogeneities emerge in the sur-

face; in particular, $5\,\mu$m bulges form in the surface above the crevice sites, forming multiple peaks. These bulges are reminiscent of the bubble instabilities previously described by Shibayama *et al* and Boudaoud *et al*[22,48], who observed pockets of gel whose polymer volume fraction ϕ is lower than the surrounding region.

To improve our understanding of the structure of these bubble features across the surface, we acquired top-view fluorescence images of gels relaxing at T_{sp}=34 °C and 36 °C. The full dataset is shown in ESI†(Fig S2B) while a representative image taken at t=200 s is shown in Fig 3B. For T_{sp}=36 °C, a noticeable line of bubbles spanning a width of $\approx$170 μm (appearing as regions with lower fluorescence intensity) emerges at the crevice sites. Features at this scale are not observed for T_{sp}=34 °C. Finally, we also employ confocal microscopy in reflection mode, which enables us to obtain more information about the topography and composition of the sample through the intensity of incident light that is reflected off the surface. These images are included in ESI†(Fig S2B). Images acquired in this manner for T_{sp} =36 °C also exhibit brightly reflecting spots corresponding to bubble formation, which do not appear when T_{sp} =34 °C, again indicating qualitatively different behavior in the gel when the surface undergoes inversion at T_{sp}=34 °C vs T_{sp}=36 °C.

To gain insight into the formation of these transient mechanical instabilities and in particular, the role of topographical confinement, we compare the polymer distribution and stress state within the gel as it is heated to 34 °C and 36 °C using finite element simulations. We adopt the equilibrium configuration of the swollen gel at 22 °C and increase the system temperature rapidly at a rate of 1 °C per 20 time steps (corresponding to 5 °C/min in reality) to either T_{sp} =34 °C or 36 °C.

Our results, shown in Fig 3C, clearly indicate differences in the polymer distribution during the gel collapse process under the two different heating paths. When the system is allowed to relax at 34 °C, we observe that the gel begins to contract from the bump sites, with ϕ between 7 and 13 % throughout the whole process of inversion. On the other hand, when the system relaxes at T_{sp} = 36 °C, we observe the formation of a very thin skin layer (a single grid cell thick) at the surface of the gel with polymer volume fraction $\phi \approx 43\%$. Just underneath it, ϕ ranges from $\approx$ 12% close to the bump sites to $\approx$ 7% at the crevice sites. We posit that this gradient in polymer concentration causes water to be preferentially squeezed laterally toward the crevice sites rather than through the skin layer, causing pressure to build up at the crevice sites. Eventually, hydrostatic pressure causes water to bulge through the skin layer, forming bubbles. Thus, topographical confinement forces bubbles to form in a very well-defined strip of $\approx$ 170μm centered around the crevice sites. This physical picture is supported by the hydrostatic pressure gradient present within the gel during the process of gel collapse, as shown in Fig 3D. (See ESI for details of the calculation.) Though skin layer formation has previously been proposed in the literature[22], this study is, to the best of our knowledge the first to visualize this process and measure the hydrostatic stress distribution within the gel through finite element simulation.

Finally, to assess the effect of the underlying topography on the formation of the skin layer, we conducted similar simulations on gels of uniform thickness (150 μm) attached to flat rigid substrates instead of topographically bumpy substrates. Notably, while a skin layer also forms on a gel confined to a flat surface, the formation of a full phase-separated layer is delayed by 10 frames (i.e. $\approx$13 s) on the gel confined to a flat rigid substrate, suggesting that topographical confinement promotes the formation of the skin layer.

3.3 Surface inversion along different temperature paths affects the process of gravity-induced particle assembly.

Next, we consider the effect of transient surface morphologies on the interfacial properties of the surface. Through confocal microscopy and finite element simulations, we observed that gradients in surface curvature change dynamically according to the thermal history of the surface. Curvatures at the length scale of 10 μm to 100 μm have all been shown to be important for the interactions of surfaces with particles, microorganisms (e.g. bacteria[49,50] and microalgae[51]) and mammalian cells[52–54], and are relevant in antifouling and tissue engineering applications. We hypothesized that new dynamics could be introduced into the patterning and assembly of small particles by temperature path-dependent control over these material parameters.

Toward this end, we explored how these non-trivial transitions might be used to control gravity-assisted assembly of particulate matter. Negatively-charged, FITC-labeled fluorescent carboxylated melamine particles were deposited onto the gel surface in a thin microchamber, and the spatial distribution of particles was monitored through fluorescence imaging as the chamber was heated from T=22 °C to T_{sp} =33 °C, 34 °C and 36 °C at R=5 °C/min (Fig 4). At 22 °C, particles sediment at the bump sites (Fig 4A-B). For T_{sp} =33 °C and R=5 °C/min, particles remain at the bump site as the surface remains relatively flat, and the gravitational force acting on the particles is insufficient to overcome particle-surface friction. For T_{sp}=34 °C, due to the low adhesion of the surface provided by the PEGDA crosslinker within the gel, the majority of particles (>60%) move to the crevice sites (Fig 4C). For T_{sp} = 36 °C, particles temporarily divide into 2 lines due to the transient physical barriers imposed by the bubble morphologies. These lines of particles gradually merge over the course of 30 min. Videos for T_{sp} = 34 °C and T_{sp} = 36 °C are provided along with the sideview of topography in ESI†Movie 1 and 2. In a separate set of experiments, we confirmed that gravity is the dominant driving force for particle movement as the maximum rate of particle motion measured for a series of charge-stabilized particles was proportional to the density of the particle (for ρ=1.01 to 2.5 g/ml) and local slope of the surface. A key feature of this process is that both the macroscopic inversion of the surface and the formation of microscopic, 5 μm high bubble instabilities is important for the diversity of particle behaviors observed. Thus, we show how temperature-path dependent surface transformations influence the process of particle assembly.

We also demonstrate a proof-of concept for how transient topographies could be used for controlling the surface aggregation of biological cells. We selected a microalgae *C.reinhardtii*, which is a model organism for microorganism adhesion[55,56] and motil-
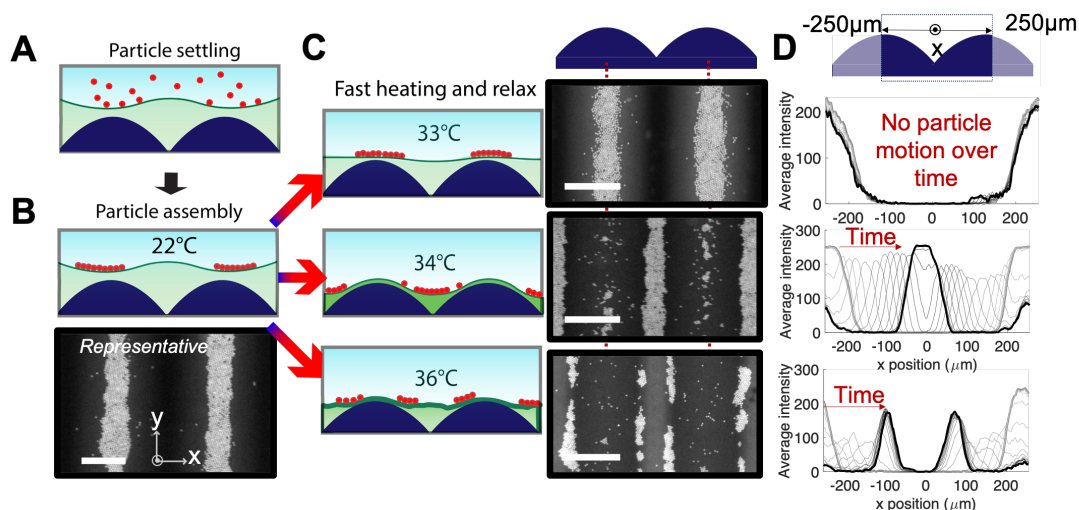
Fig. 4 Effect of transient morphologies on the gravity-assisted assembly of sedimenting particles. Both macroscopic surface inversion and formation of transient peaks affect the time-dependent accumulation behavior of particles. A. Schematic of particle settling in microchamber ($h_{chamber} \approx 350\,\mu$m). B. Schematic and representative topview fluorescence image of FITC-labeled carboxylated melamine particles accumulated at bump sites at T=22 °C. Scale: 250 μm. C. Schematic and fluorescent images of particle assembly under gravity for T_{sp}=33 °C, 34 °C, and 36 °C at 5 °C/min under the fast heating regime (5 °C/min). After the same time period of t=10 minutes, particles stay at bump sites if T_{sp}=33 °C (top), move to crevice sites if T_{sp}=34 °C (middle), or divide into two lines at positions corresponding to transient crevice coordinates if T_{sp}=36 °C (bottom). Scale: 250 μm. D. Quantification of fluorescence intensity of FITC-modified carboxylated melamine particles over one bump-to-bump period (x=−250 μm to +250 μm) between time t_0=0 min and t_f=10 min for T_{sp}=33 °C, 34 °C, and 36 °C. Grey lines denote the spatial distribution of particles at 20 second intervals between t_0=0 and t_f=10 minutes, while black lines denote where particles accumulate at t_f=10 minutes.
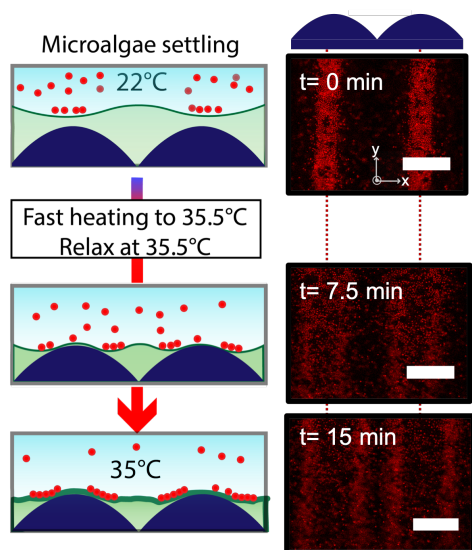
Fig. 5 Microalgae collect in transient crevice points formed by mechanical instabilities. At low temperatures, *C.reinhardtii* initially accumulate at the bump sites. When T_{sp}=35 °C and R=2.5 °C/min, microalgae cluster into two lines over the course of 15 minutes. This behavior is consistent with that of the non-living colloidal particles shown in Fig 4, indicating that the transient morphologies also have an effect on the assembly of biological cells. Scale: 250 μm

ity[51] studies. Mediated by the presence of two long flagella ($\approx$ 10μm in length), *C.reinhardtii* cells exhibit a wide range of active behaviors such as surface adhesion[55], phototaxis[57], and sensitivity to curvature[51]. The chlorophyll of algal cells can be clearly visualized through fluorescence confocal microscopy, as shown in Fig 5. First, we allowed the cells to settle on the surface for 15 mins. Similarly to carboxylated melamine particles, at 22 °C a fraction of *C.reinhardtii* cells initially settled at the epoxy bump sites between protruding gel bumps. Next, we visualized the behavior of cells during a fast ramp temperature sequence. In order to reduce thermal shock of the algae, the heating rate was reduced to R=2.5 °C/min. At this heating rate, the surface reaches 35.5 °C within 5.2 min, and the surface deformation rate is still limited by gel diffusion and skin layer formation. Upon increasing the temperature to T_{sp}=35.5 °C, *C.reinhardtii* cells gradually assemble onto the surface and aggregate in the transient crevices on either side of the bump sites over the course of 15 min.

We posit that at least a subset of microalgae in our experiments initially accumulate at the bump sites due to a lack of functioning flagella, thus migrating into the crevices as passive particles. However, for flagella-bearing cells, it is possible that the concavity in that region presents a favorable location to migrate and accumulate[51], but not adhere strongly. In general, thick polyethylene-glycol-containing gels have previously been observed to resist early adhesion of other flagella-bearing microorganisms such as *E.coli*[58]. We hypothesize that upon increasing the temperature, the spontaneous aggregation of algae into the dynamic crevices is caused by a combination of effects that are dominated by topographically driven changes in flow over the surface and an in-

crease in the adhesive properties of the gel, as evidenced by an increase in polymer volume fraction. The dynamic change in surface topography could also be accompanied by spatial changes in environmental cues such as curvature or light that drive motility in *C.reinhardtii* [51,57]. While the precise mechanism is beyond the scope of this study, this result indicates that transient topographical changes can be harnessed for the movement and assembly of biological cells.

It is noteworthy that while the presented results show the emergence of transient morphologies obtained during the heating process, non-equilibrium topographical transitions occur and can also be harnessed for controlling particle assembly during the cooling process. Details for surface morphologies obtained under two different cooling rates: R=0.2 °C/min and 5 °C/min and associated results for particle assembly are shown in ESI†(Fig S3).

3.4   Designing more complex particle trajectories through patterning preswollen gel height

In the previous sections, we demonstrated how non-equilibrium mechanical instabilities formed as a result of rapid heating introduce transient dynamics into the gravitational assembly of particles and microalgae. Thus far, the formation of non-equilibrium morphologies has been exclusively confined to a narrow strip at the crevice sites. We attribute the lack of bubble formation at the bump sites to the higher polymer density within the gel at bump sites at the onset of skin layer formation, preventing water from being driven to those regions under hydrostatic pressure gradients. Thus, we hypothesized that the zone of mechanical instabilities could be expanded by increasing the thickness of preswollen gel at the bump sites (h_{bump}). To visualize the effect of increasing h_{bump} in a single sample, we used a slightly angled confining cover slip during synthesis and created a surface where h_{bump} varied linearly from $<10\,\mu$m on one end to $60\,\mu$m at the other end. This data is included in ESI†(S4A-B). A series of top-view fluorescent images from t=0 to 10 min showed that when such samples were heated to $T_{sp} = 36$ °C at R=5 °C/min, instabilities appeared at the bump sites only when $h_{bump} > 50\,\mu$m. We used this threshold to create an independent sample with $h_{bump} = 50\,\mu$m to obtain a more high-resolution image (Fig 6A, top). Indeed, a representative image taken at t=7 min after heating the sample to $T_{sp} = 36$ °C at R=5 °C/min shows a clear presence of a column of water-filled bubbles at the bump sites (Fig 6A, bottom). The full timelapse is presented in ESI†(Fig S4C). The particle assembly on such a surface follows faithfully the emergence of the bubbles: In this case, we observe that the particles are temporarily scattered into the transient crevices that form on either side of the bump sites (Fig 6B).

4   Conclusions

In this article, we used confocal microscopy and finite element simulations to show how confining a gel to a topographically patterned substrate enables us to create a surface whose topography can be inverted with temperature through a number of different transient morphologies as a function of heating path. These pathway-dependent transient states are caused by spatial gradi-
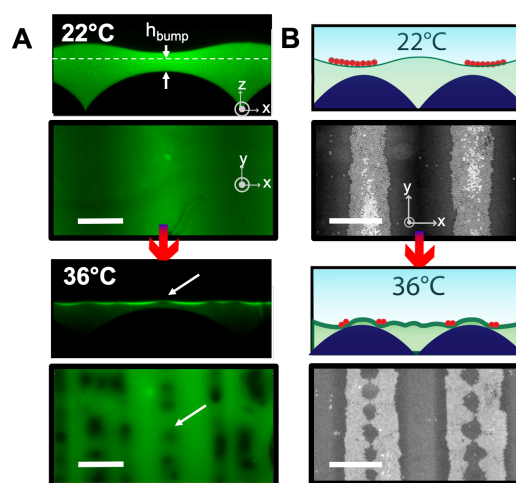
Fig. 6 Effect of increasing preswollen gel height h_{bump} on the formation of mechanical surface instabilities at the bump sites. A. When surfaces fabricated with h_{bump}=50 μm are heated to T_{sp}=36 °C at R=5 °C/min, bubbles appear in a line at the bump sites, as shown through sideview confocal fluorescence microscopy images. Top image: T=22 °C, t=0 min. White dotted lines delineate the preswollen gel height h_{bump}. Bottom image: T=36 °C, t=7 min. Bubble morphologies are indicated with the white arrows. Scale: 125 μm. (B) Transient bubbles formed at the bump sites can be used to pattern particle assemblies. During heating from T=22 °C to $T_{sp} = 36$ °C at R=5 °C/min, carboxylated melamine particles (white) first accumulate in the transient crevices that emerge next to the bump sites. Scale: 250 μm.

ents in the various timescales associated with gel shrinking, and can be used to control the assembly process of colloidal particles and microalgae. Furthermore, more complex, non-equilibrium surface transformations can be programmed by tuning the height of the gel patterned over the surface. We suggest, therefore, that the kinetics of stimulus-induced deformation be harnessed in the design of multifunctional, actuatable hybrid surfaces. In particular, by exploring different kinetic regimes, it is possible to access a range of non-trivial transient states and associated material properties. This presents intriguing opportunities for creating surfaces whose topographies and properties can be tuned by stimuli history. Moving forward, we envision that this behavior can be combined with other switchable features of stimuli-responsive gels to generate stimuli history-dependent functionality in smart actuators, regulators, switchable adhesives and antifouling surfaces, as well as drug-eluting, stimuli-indicating and sensing devices.

Conflicts of interest

There are no conflicts to declare.

Acknowledgements

Notes and references

1 M. a. C. Stuart, W. T. S. Huck, J. Genzer, M. Müller, C. Ober, M. Stamm, G. B. Sukhorukov, I. Szleifer, V. V. Tsukruk, M. Urban, F. Winnik, S. Zauscher, I. Luzinov and S. Minko, *Nature materials*, 2010, **9**, 101–113.

2 M. Wei, Y. Gao, X. Li and M. J. Serpe, *Polymer Chemistry*, 2017, **8**, 127–143.

3 T. Manouras and M. Vamvakaki, *Polymer Chemistry*, 2017, **8**, 74–96.

4 V. Luchnikov, L. Ionov and M. Stamm, *Macromolecular Rapid Communications*, 2011, **32**, 1943–1952.

5 L. Ionov, *Materials Today*, 2014, **17**, 494–503.

6 Z. Liu, W. Wang, R. Xie, X. J. Ju and L. Y. Chu, *Chemical Society Reviews*, 2016, **45**, 460–475.

7 A. B. Croll, N. Hosseini and M. D. Bartlett, *Advanced Materials Technologies*, 2019, **1900193**, 1–20.

8 X. Li, B. Wu, H. Chen, K. Nan, Y. Jin, L. Sun and B. Wang, *Journal of Materials Chemistry B*, 2018, **6**, 4274–4292.

9 H. Kuroki, I. Tokarev and S. Minko, *Annual Review of Materials Research*, 2012, **42**, 343–372.

10 C. de Las Heras Alarcon, S. Pennadam and C. Alexander, *Chemical Society reviews*, 2005, **34**, 276–285.

11 W. Li, Z. Yan, J. Ren and X. Qu, *Chemical Society reviews*, 2018, **47**, 8639–8684.

12 S. J. Jeon, A. W. Hauser and R. C. Hayward, *Accounts of Chemical Research*, 2017, **50**, 161–169.

13 P. Kim, L. D. Zarzar, X. He, A. Grinthal and J. Aizenberg, *Solid state & Mat Sci*, 2011, **15**, 236–245.

14 Y. Tokudome, H. Kuniwaki, K. Suzuki, D. Carboni, G. Poologasundarampillai and M. Takahashi, *Advanced Materials Interfaces*, 2016, **3**, 1500802.

15 A. Sutton, T. Shirman, J. V. I. Timonen, G. T. England, P. Kim, M. Kolle, T. Ferrante, L. D. Zarzar, E. Strong and J. Aizenberg, *Nature Communications*, 2017, **8**, 14700.

16 Y. Liu, G. McFarlin, X. Yong, O. Kuksenok and A. C. Balazs, *Langmuir*, 2015, **31**, 7524–7532.

17 M. C. Koetting, J. T. Peters, S. D. Steichen and N. A. Peppas, *Materials Science and Engineering R: Reports*, 2015, **93**, 1–49.

18 W. Chen, L. Qu, D. Chang, L. Dai, S. Ganguli and A. Roy, *Chemical Communications*, 2008, 163–5.

19 J. Kim, J. Yoon and R. C. Hayward, *Nature materials*, 2010, **9**, 159–64.

20 J. E. Stumpel, B. Ziółkowski, L. Florea, D. Diamond, D. J. Broer and A. P. H. J. Schenning, *ACS Applied Materials and Interfaces*, 2014, **6**, 7268–7274.

21 J. Dervaux and M. B. Amar, *Annual Review of Condensed Matter Physics*, 2012, **3**, 311–332.

22 M. Shibayama and K. Nagai, *Macromolecules*, 2000, **32**, 7461–7468.

23 J. I. Maskawa, T. Takeuchi, K. Maki, K. Tsujii and T. Tanaka, *Journal of Chemical Physics*, 1999, **110**, 10993–10999.

24 T. Okajima, I. Harada, K. Nishio and S. Hirotsu, *Journal of Chemical Physics*, 2002, **116**, 9068–9077.

25 T. Shen, J. Kan, E. Benet and F. J. Vernerey, *Soft Matter*, 2019, **15**, 5842–5853.

26 T. Tanaka, S.-t. Sun, Y. Hirokawa and T. Amiya, *Nature*, 1986, **325**, 7–9.

27 E. S. Matsuo and T. Tanaka, *J. Chem. Phys.*, 1990, **89**, 1695–1703.

28 Y. Li, C. Li and Z. Hu, *The Journal of Chemical Physics*, 1994, **100**, 4637–4644.

29 Y. W. Chang, M. S. Dimitriyev, A. Souslov, S. V. Nikolov, S. M. Marquez, A. Alexeev, P. M. Goldbart and A. Fernández-Nieves, *Physical Review E*, 2018, **98**, 1–5.

30 F. Dalier, F. Eghiaian, S. Scheuring, E. Marie and C. Tribet, *Biomacromolecules*, 2016, **17**, 1727–1736.

31 E. Svetushkina, N. Puretskiy, L. Ionov, M. Stamm and A. Synytska, *Soft Matter*, 2011, **7**, 5691.

32 W. Wang, J. V. Timonen, A. Carlson, D. M. Drotlef, C. T. Zhang, S. Kolle, A. Grinthal, T. S. Wong, B. Hatton, S. H. Kang, S. Kennedy, J. Chi, R. T. Blough, M. Sitti, L. Mahadevan and J. Aizenberg, *Nature*, 2018, **559**, 77–82.

33 I. Banerjee, R. C. Pangule and R. S. Kane, *Advanced Materials*, 2011, **23**, 690–718.

34 L. Wondraczek, G. Pohnert, F. H. Schacher, A. Köhler, M. Gottschaldt, U. S. Schubert, K. Küsel and A. A. Brakhage, *Advanced Materials*, 2019, **31**, 1–14.

35 K. H. Son and J. W. Lee, *Materials*, 2016, **9**, 1–13.

36 J. Es Sayed, C. Lorthioir, P. Perrin and N. Sanson, *Soft Matter*, 2019, **15**, 963–972.

37 M. Ciftci, M. U. Kahveci, Y. Yagci, X. Allonas, C. Ley and H. Tar, *Chemical Communications*, 2012, **48**, 10252–10254.

38 O. Kuksenok, V. V. Yashin and A. C. Balazs, *Physical Review E*, 2008, **78**, year.

39 V. V. Yashin and A. C. Balazs, *Journal of Chemical Physics*, 2007, **126**, year.

40 T. Zhang, V. V. Yashin and A. C. Balazs, *Soft Matter*, 2018, **14**, 1822–1832.

41 C. M. Nolan, C. D. Reyes, J. D. Debord, A. J. García and L. A. Lyon, *Biomacromolecules*, 2005, **6**, 2032–2039.

42 B. Sierra-Martín, Y. Laporte, A. B. South, L. A. Lyon and A. Fernández-Nieves, *Physical Review E - Statistical, Nonlinear, and Soft Matter Physics*, 2011, **84**, 1–4.

43 M. Dušková-Smrčková and K. Dušek, *ACS Macro Letters*, 2019, **8**, 272–278.

44 E. Sato Matsuo and T. Tanaka, *The Journal of Chemical Physics*, 1988, **89**, 1695–1703.

45 A. Boudaoud and S. Chaïeb, *Physical Review E - Statistical Physics, Plasmas, Fluids, and Related Interdisciplinary Topics*, 2003, **68**, 6.

46 S. Hirotsu and A. Onuki, *Journal of the Physical Society of Japan*, 1989, **58**, 1508–1511.

47 S. Cai and Z. Suo, *Journal of the Mechanics and Physics of Solids*, 2011, **59**, 2259–2278.

48 A. Boudaoud, *Physical Review E*, 2003, **68**, 1–6.

49 R. J. Crawford, H. K. Webb, V. K. Truong, J. Hasan and E. P. Ivanova, *Advances in Colloid and Interface Science*, 2012, **179-**

182, 142–149.

50 R. Mok, J. Dunkel and V. Kantsler, *Physical Review E*, 2019, **99**, 52607.

51 T. Ostapenko, F. J. Schwarzendahl, T. J. Böddeker, C. T. Kreis, J. Cammann, M. G. Mazza and O. Bäumchen, *Physical Review Letters*, 2018, **120**, 68002.

52 K. S. Cannon, B. L. Woods and A. S. Gladfelter, *Trends in Biochemical Sciences*, 2018, **42**, 961–976.

53 A. Beber, C. Taveneau, M. Nania, F. C. Tsai, A. Di Cicco, P. Bassereau, D. Lévy, J. T. Cabral, H. Isambert, S. Mangenot and A. Bertin, *Nature Communications*, 2019, **10**, 1–12.

54 N. D. Bade, T. Xu, R. D. Kamien, R. K. Assoian and K. J. Stebe, *Biophysical Journal*, 2018, **114**, 1467–1476.

55 C. T. Kreis, A. Grangier and O. Bäumchen, *Soft Matter*, 2019, **15**, 3027–3035.

56 C. T. Kreis, M. Le Blay, C. Linne, M. M. Makowski and O. Bäumchen, *Nature Physics*, 2018, **14**, 45–49.

57 R. L. Stavis and R. Hirschberg, *Journal of Cell Biology*, 1973, **59**, 367–377.

58 K. W. Kolewe, J. Zhu, N. R. Mako, S. S. Nonnenmann and J. D. Schiffman, *ACS Applied Materials and Interfaces*, 2018, **10**, 2275–2281.

Patterning temperature-responsive gels on topographically structured substrates enables multiple heating path-dependent transformations between two inverted topographies.